

1 **Timing of crystallisation of the Lunar Magma Ocean constrained by**
2 **the oldest zircon**

3

4 A. Nemchin¹, N. Timms¹, R. Pidgeon¹, T. Geisler², S. Reddy¹ and C.Meyer³

5 ¹*Department of Applied Geology, Western Australian School of Mines, Curtin*

6 *University of Technology, Bentley, Western Australia, 6102, Australia*

7 ²*Institut für Mineralogie, Westfälische Wilhelms-Universität, Corrensstr 24, 48149,*

8 *Münster, Germany.*

9 ³*NASA Johnson Space Center, Houston, Texas, 77058*

10

11 **The presently favoured concept for the early evolution of the Moon involves**
12 **consolidation of debris from a giant impact of a Mars sized body with Earth**
13 **forming a primitive Moon with a thick global layer of melt referred to as the**
14 **Lunar Magma Ocean¹. It is widely accepted that many significant features**
15 **observed on the Moon today are the result of crystallisation of this magma ocean.**
16 **However, controversy exists over the precise timing and duration of the**
17 **crystallisation process. Resolution of this problem depends on the establishment**
18 **of precise and robust key crystallisation time points. We report a 4417±6 Myr**
19 **old zircon in lunar breccia sample 72215,195, which provides a precisely**
20 **determined younger limit for the solidification of the Lunar Magma Ocean. A**
21 **model based on these data, together with the age of the Moon forming giant**
22 **impact, defines an exponential time frame for crystallisation and suggests**
23 **formation of anorthositic crust after about 80-85% of the magma ocean was**
24 **solidified. In combination with other zircon ages the 4417 ± 6 Myr age also**

25 **suggests that the very small (less than a few per cent) residual portion of the**
26 **magma ocean continued to solidify during the following 300-500 m.y.**

27 Fractional crystallisation of the Lunar Magma Ocean (LMO) involved the
28 early density-driven separation of mafic cumulates and flotation of a plagioclase-rich
29 lunar crust represented by ferroan-anorthosite¹. Subsequent crystallisation of ilmenite
30 from the remaining portion of the LMO¹ left a residual liquid enriched in highly
31 incompatible elements. This liquid formed the enriched reservoir referred to as
32 urKREEP (from high concentrations of K, REE, and P)².

33 A precise determination of the timing of fractional crystallisation of the LMO
34 has been inhibited by the susceptibility of Sm-Nd and other systems to the partial
35 resetting during the later thermal pulses associated with the meteorite impacts. As a
36 result, the Sm-Nd mineral isochrons constrained for the ferroan-anorthosite samples
37 show wide spread of ages between 4.56 ± 0.07 Byr (Ref. 3) and 4.29 ± 0.06 Byr (Ref. 4).
38 The best estimate for the age of ferroan anorthosites determined as 4456 ± 40 Myr from
39 the combination of mafic minerals in all analysed samples but excluding plagioclase
40 data that are partially disturbed⁵ has another inherited problem as it assumes that all
41 samples have been formed at the same time.

42 Another way that has been used to constrain the timing of the LMO
43 differentiation is via model ages of rocks derived from different reservoirs in the lunar
44 mantle. In particular, a KREEP-rich source is recognised as an essential part of late
45 stage crystallisation of the LMO, and model ages of urKREEP formation have been
46 estimated as ~ 4.6 Byr by Rb-Sr analysis of lunar soils⁶, ~ 4.42 Byr from U-Pb
47 systematics of highlands rocks and a basalt sample⁷ and ~ 4.36 Byr from the Sm-Nd
48 model ages of KREEP samples⁸. An average of model age for KREEP was estimated
49 as 4.42 ± 0.07 Byr (1σ uncertainty)⁹. Recent W isotope data on metals from low and

50 high-Ti mare basalts as well as two KREEP-rich samples¹⁰ suggest that the last
51 equilibration of the LMO, which is only possible up to a critical point when about
52 60% of the melt is solidified, occurred after 4507 Myr (60 m.y. after formation of the
53 Solar System). This result is in agreement with ¹⁴⁶Sm-¹⁴²Nd model age of the LMO¹⁰,
54 which is based on the combined ¹⁴⁷Sm-¹⁴³Nd and ¹⁴⁶Sm-¹⁴²Nd systems in lunar basalts
55 and implies a 238^{+56}_{-40} m.y. (Ref. 11) to 215^{+23}_{-21} m.y. (Ref. 12) time interval for lunar
56 mantle formation. Despite the general agreement between the model ages determined
57 using different isotope systems their accuracy is limited by the models and the timing
58 of LMO remains loosely constrained to the first 250 m.y. of lunar history.

59 Both isotopic resetting and model dependence problems associated with
60 numerous previous attempts to place limits on the time of LMO crystallisation can be
61 avoided by using U-Pb system in zircon^{13, 14}, which is well known for its stability
62 under a variety of extreme conditions. Growth of zircon in melts is governed by
63 zircon saturation, which can only be achieved in a mafic magma initially enriched in
64 Zr (Ref. 15). Consequently, the presence of zircon in the lunar samples is linked to the
65 initial enrichment of the magma in the KREEP component (i.e., urKREEP must form
66 on the Moon before zircon can appear in any rock type). Therefore, the oldest zircon
67 defines a younger limit for the time of urKREEP formation.

68 Here we report the oldest zircon crystal found on the Moon so far, which is
69 located in the matrix of Apollo 17 clast-rich impact melt breccia 72215, in the thin
70 section 72215, 195. The 0.5 mm grain lacks well developed crystal faces and contains
71 several brittle fractures (Fig. 1), and we thus consider it to be a relict fragment of a
72 larger grain that was incorporated into the host breccia.

73 Forty one SIMS U-Pb analyses were made on this grain (Tab. 1, Fig. 2a). The
74 results indicate a complex pattern of isotope resetting that systematically varies with

75 the microstructural features of the grain (Tab. 1; Fig. 1). These microstructural
76 features are a combination of primary magmatic characteristics and different degree of
77 self-irradiation damage highlighted by the variable birefringence and
78 cathodoluminescence (CL) emission, as well as deformation patterns revealed by
79 crystallographic orientation analysis of electron backscatter diffraction (EBSD)
80 patterns. The observed overall decrease in $^{207}\text{Pb}/^{206}\text{Pb}$ ages correlated with an increase
81 of the local misorientation determined for each SHRIMP spot¹⁶ (Fig. 2b), indicates
82 that this differential resetting of U-Pb system occurred as a result of impact-related
83 plastic deformation, an interpretation that is consistent with trace element variations
84 recorded in other deformed zircons^{16, 17}

85 All 41 U-Pb analyses are distributed along concordia between 4418 ± 8 and
86 4331 ± 16 Myr (uncertainties are 2σ) (Fig. 2a). The four oldest analyses, from
87 undeformed parts of the grain, form a coherent group on a concordia plot (Fig. 2a)
88 with concordia intercept at 4420 ± 15 Myr and an average $^{207}\text{Pb}/^{206}\text{Pb}$ age of 4417 ± 6
89 Myr. We interpret this age as the age of zircon crystallisation. The five youngest
90 analyses form a coherent group in the $^{207}\text{Pb}/^{206}\text{Pb}$ vs. $^{238}\text{U}/^{206}\text{Pb}$ diagram (Fig. 2a),
91 defining a concordia intercept age of 4334 ± 10 Myr for the common Pb uncorrected
92 data and average $^{207}\text{Pb}/^{206}\text{Pb}$ age of 4333 ± 7 Myr for the Stacey-Kramers modern Pb
93 corrected data. These analyses correspond to areas of moderate luminescence, good
94 EBSD pattern quality and low U and Th concentrations (Fig. 1). Importantly, these
95 analyses are also from areas where the deformation bands intersect and/or have high
96 misorientation, suggesting deformation-related Pb-loss. It is evident that the most
97 deformed areas of the grain have suffered the greatest Pb loss, and we interpret the
98 concordia intersection age as a reflection of mobility of the U-Pb system in the grain
99 during an impact, although the resetting can be incomplete. The remaining

100 intermediate ages are from areas of moderately-strained parts of the grain, and likely
101 reflect a partial resetting of U-Pb system.

102 Our results indicate that the urKREEP source formed by 4417 ± 6 Myr and it
103 follows that crystallisation of the LMO was almost completed by this time. The zircon
104 age is almost 100 Ma older than the age calculated from combined ^{142}Nd - ^{143}Nd
105 systematics of lunar basalts and highland rocks^{11, 12}. These later estimates, however,
106 are based on the assumption that the separate mantle reservoirs have been formed at
107 the same time and had similar initial isotopic compositions of Nd. This may not be the
108 case, even for KREEP magmas and the source of high-Ti basalts. Both formed last in
109 the LMO crystallisation sequence and largely define the slope of combined ^{142}Nd -
110 ^{143}Nd isochrones. Nevertheless, the formation of urKREEP source at 4417 ± 6 Myr is
111 in agreement with the age of 4456 ± 40 Myr determined for the ferroan anorthosite
112 samples⁵, even though the ages are not completely resolved within the errors.

113 A combination of the urKREEP minimum formation age of 4417 ± 6 Myr and
114 other data reflecting different stages of LMO evolution allows us to model the history
115 of magma ocean differentiation and crystallisation on the Moon, and two end-
116 members are presented (Fig. 3). Both models are constrained by the new 4417 ± 6 Myr
117 zircon age, defining a minimum age for formation of Lunar urKREEP at a late stage
118 in the crystallisation of the LMO. Both are also based on the assumption that the
119 LMO formed as a result of fast accretion following the giant impact¹ and, therefore,
120 the age of LMO formation is similar to the age of the Moon. The best current estimate
121 of the age of the giant impact based on the Hf-W data is 62^{+90}_{-10} m.y. after the
122 formation of the Solar System¹⁰. These data place an older limit of LMO formation of
123 50 m.y. after the first condensation in the Solar Nebula (i.e. 4517 Myr). A simple
124 model of LMO evolution (Fig.3, solid line) suggests a sequential fractionation of

125 olivine \rightarrow orthopyroxene \pm olivine \rightarrow olivine + clinopyroxene \pm plagioclase \rightarrow
126 clinopyroxene + plagioclase \rightarrow clinopyroxene + plagioclase + ilmenite assemblages.
127 However, the assumption of sequential fractionation of mineral phases throughout the
128 whole LMO is probably an oversimplification because it is likely that: (i) a significant
129 temperature difference would exist between the lower and upper parts of the LMO;
130 (ii) the appearance of different minerals on the liquidus is unlikely to be
131 contemporaneous in different parts of the magma ocean; (iii) convection can prevent
132 effective removal of minerals from the liquid; and (iv) the formation of an insulation
133 lid can change cooling regime of the LMO. A more complex models of LMO
134 crystallisation (Fig.3, dashed line) involves rapid initial cooling of the magma ocean
135 as a result of vigorous turbulent convection¹⁸, which results in solidification of
136 substantial proportion of LMO without significant fractionation. This was followed by
137 fractionation limited to the relatively thin top layer of the LMO due to much slower
138 cooling resulting from a less vigorous convection regime, and possibly formation of a
139 thermally insulating surface lid.

140 Nevertheless, both models combined with the available chronological data
141 suggest that ilmenite bearing cumulates precipitated after about 90% of LMO
142 crystallisation, leaving a few percent of residual KREEP melt by 4417 ± 6 Myr. These
143 data suggest that the main volume of the LMO solidified within about 100 m.y. The
144 age distribution patterns obtained for numerous zircon grains from Apollo 17 and 14
145 breccias¹⁴ suggest that the residual small volume fraction of the LMO liquid could
146 have cooled slowly over the subsequent 400 to 500 m.y., probably sustained by the
147 internal heating related to radioactive decay. These patterns indicate gradual shrinking
148 of a semi-molten KREEP reservoir towards the centre of Procellarum KREEP
149 terrane¹⁴, and that by about 4.25 Byr the KREEP reservoir solidified under the area

150 occupied by the Serenitatis basin, but continued to be active closer to the middle of
151 Procellarum KREEP terrane near the Imbrium basin until about 3.90 Byr ago.
152 Assuming that the thickness of the KREEP source is approximately constant
153 throughout the Procellarum terrane, this accounts for an additional reduction in the
154 residual proportion of KREEP melt of about 50% by 4.25 Byr.

155 Despite the precise fixation of the timing of the last stage of LMO
156 crystallisation by our results, the timing of plagioclase appearance in the
157 crystallisation sequence remains imprecise. Estimates for the appearance of
158 plagioclase on the liquidus vary from about 60% to 80% of LMO crystallisation,
159 depending on the assumed bulk Al content of the LMO ^{19, 20}. Assuming sequential
160 crystallisation of minerals (Fig. 3, solid line) and using available geochronological
161 data for the ferroan anorthosite samples, 70% of crystallisation of LMO is necessary
162 before plagioclase can become a liquidus phase. In the more complex model (Fig. 3,
163 dashed line), the lunar crust formed after crystallisation of 80-85% of the LMO.
164 However, both estimates are within the uncertainties associated with the relatively
165 imprecise estimate of age of the ferroan anorthosites. The large uncertainty of these
166 age also results in the large range (anywhere between 20 and 100 my) for the possible
167 duration of plagioclase flotation. As a result, further refinement of the models awaits
168 more precise determination of the age of Lunar anorthosite formation.

169

170 **(1995 words)**

171

172 **Methods summary**

173 The sample is a polished thin section of breccia 72215 prepared by NASA. The
174 microstructure of the zircon was characterized by SEM-based cathodoluminescence

175 imaging and electron backscatter diffraction (EBSD) mapping using the facilities at
176 Curtin University of Technology, Perth, Western Australia. Collection of EBSD data
177 was processed using the procedures optimised for zircon²¹. Slip systems were
178 resolved from crystallographic orientation data using simple geometric models of
179 low-angle boundaries¹⁷.

180 U-Pb data were obtained using Sensitive High Resolution Ion Microprobe (SHRIMP)
181 at the John de Laeter Centre of Mass Spectrometry, Curtin University of Technology
182 following the standard analytical procedure described elsewhere¹³. Pb-U ratios were
183 normalised to the 564 Ma Sri-Lankan zircon CZ3 analysed in a separate mount.
184 Common Pb was corrected using modern Stacey and Kramers lead, following the
185 conclusion that substantial proportion of common Pb in the lunar thin sections results
186 from the surface contamination¹⁴. Regardless, of the selection of common Pb for the
187 correction, very low proportion of ²⁰⁴Pb in the thin section 72215,195 makes the
188 calculated ages insensitive to the uncertainty in the common Pb.

189 **(176 words)**

190

191 **References**

- 192 1. Shearer, C.K., Hess, P.C., Wieczorek, M.A., Pritchard, M.E., Parmentier, E.M.,
193 Borg, L.E., Longhi, J., Elkins-Tanton, L.T., Neal, C.R., Antonenko, I., Canup, R.M.,
194 Halliday, A.N., Grove, T.L., Hager, B.H., Lee, D-C., & Wiechert, U. Thermal and
195 Magmatic Evolution of the Moon, *In: New Views of the Moon; Rev. Mineral.*
196 *Geochem., Mineralogical Society of America* **60**, 365-518, 2006.
- 197
- 198 2. Warren, P.H. & Wasson, J.T. The origin of KREEP. *Rev Geophys Space Phys* **17**,
199 73-88, 1979.

200

201 3. Alibert, C, Norman, M.D.& McCulloch, M.T. An ancient Sm-Nd age for a ferroan
202 noritic anorthosite clast from lunar breccia 67016. *Geochim Cosmochim Acta* **58**,
203 2921-2926, 1994.

204

205 4. Borg, L., Norman, M., Nyquist, L.E., Bogard, D.D., Snyder, G., Taylor, .L, &
206 Lindstrom M.M. Isotopic studies of ferroan anorthosite 62236: a young lunar crustal
207 rock from a light rare-earth-element-depleted source. *Geochim Cosmochim Acta* **63**,
208 2679-2691, 1999.

209

210 5. Norman, M.D., Borg, L.E., Nyquist, L.E. & Bogard, D.D. Chronology,
211 geochemistry, and petrology of a ferroan noritic anorthosite from Descartes breccia
212 67215: Clues to the age, origin, structure and impact history of the lunar crust.
213 *Meteoritics & Planet. Sci.* **38**, 645-661, 2003.

214

215 6. Papanastassiou, D.A., Wasserburg, G.J. & Burnett, D.S. Rb-Sr ages of lunar rocks
216 from the see of Tranquillity. *Earth and Panet. Sci. Lett.* **8**, 1-19, 1970.

217

218 7. Tera, F. & Wasserburg, G. U-Th-Pb systematics on lunar rocks and inferences
219 about lunar evolution and the age of the moon. *Proc. 5th Lunar Sci. Conf.*, 1571-
220 1599, 1974.

221

222 8. Lugmair, G.W., & Carlson, R.W. The Sm-Nd history of KREEP. *Proc Lunar*
223 *Planet Sci Conf 9*, 689-704, 1978.

224

- 225 9. Nyquist, L.E. & Shih, C.-Y. The isotopic record of lunar volcanism. *Geochim.*
226 *Cosmochim. Acta* **56**, 2213-2234, 1992.
- 227
- 228 10. Touboul, M., Kleine, T., Bourdon, B., Palme, H. & Wieler, R. Late formation and
229 prolonged differentiation of the Moon inferred from W isotopes in lunar metals.
230 *Nature* **450**, 1206-1209, 2007.
- 231
- 232 11. Nyquist, L.E., Wiesmann, H., Shih, C.-Y., Keith, J.E. & Harper, C.L. ^{146}Sm - ^{142}Nd
233 formation interval in the lunar mantle. *Geochim Cosmochim Acta* **59**, 2817-2837,
234 1995.
- 235
- 236 12. Rankenburg, K., Brandon, A.D. & Neal, C. Neodymium isotope evidence for the
237 chondritic composition of the Moon, *Science* **312**, 1369-1372, 2006.
- 238
- 239 13. Compston, W., Williams, I.S. & Meyer, C. U-Pb geochronology of zircons from
240 Lunar Breccia 73217 using a sensitive high mass-resolution ion microprobe, *Proc.*
241 *Lunar Planet. Sci. Conf. 14th*, *J. Geophys. Res.* **89**, B525-534, 1984.
- 242
- 243 14. Nemchin, A.A., Pidgeon, R.T., Whitehouse, M.J., Vaughan, J.P. & Meyer, C.
244 SIMS U-Pb study of zircon from Apollo 14 and 17 breccias: Implications for the
245 evolution of lunar KREEP, *Geochim. Cosmochim. Acta.* **72**, 668-689, 2008.
- 246
- 247 15. Dickinson, J.E. & Hess, P.C. Zircon saturation in lunar basalts and granites, *Earth*
248 *Planet. Sci. Lett.* **57**, 336-344, 1982.
- 249

250 16. Timms, N.E., Kinny, P.D., & Reddy, S.M. Enhanced diffusion of Uranium and
251 Thorium linked to crystal plasticity in zircon. *Geochem. Trans.*, **7**, 10, 2006.

252

253 17. Reddy, S.M., Timms, N.E., Trimby, P., Kinny, P.D., Buchan, C., & Blake, K.
254 Crystal-plastic deformation of zircon: A defect in the assumption of chemical
255 robustness. *Geology*, **34**, 257–260, 2006.

256

257 18. Solomatov, V. S. Fluid dynamics of a terrestrial magma ocean, *In: Origin of the*
258 *Earth and Moon*, edited by R. Canup and K. Righter, University of Arizona Press,
259 Tucson, Arizona, pp. 323-338, 2000.

260

261 19. Snyder, G.A., Taylor, L.A. & Neil, C.R. A chemical model for generating the
262 sources of mare basalts: Combined equilibrium and fractional crystallization of the
263 lunar magmasphere. *Geochim Cosmochim Acta* **56**, 3809-3823, 1992.

264

265 20. Longhi J. A model of early lunar differentiation. *Proc Lunar Planet Sci Conf.* **11**,
266 289-315, 1980.

267

268 21. Reddy, S.M., Timms, N.E., Kinny, P.D., Buchan, C., & Trimby, P. Natural plastic
269 deformation of zircon and its geological significance. *Contrib. Mineral. Petrol.*, **153**,
270 625–645, 2007.

271

272 **Acknowledgements**

273 All correspondence and requests for materials should be addressed to A. Nemchin. In
274 particular we would like to thank the astronauts of Apollo 17 for risking their lives to

275 collect the sample. The project was supported by the office of R&D department at
276 Curtin University of Technology. Imaging was supported by the Australian Research
277 Council Discovery Grant DP0664078 to S. Reddy and N. Timms

278

279 **Figure captions**

280 **Figure 1. Microstructure of the zircon grain from lunar breccia 72215,195. (a)**

281 Optical photomicrograph, cross polarised light showing sector zones and faint
282 compositional growth zones (inset i); (b) panchromatic CL image with superimposed
283 mean U-Pb ages for individual SHRIMP analyses; (c) Map showing variations in
284 EBSD pattern quality (band contrast) from poor (black) to good (white); (d) Map
285 derived from EBSD data showing variations in crystallographic orientation relative to
286 the mean reference orientation (red cross).

287

288 **Figure 2. U-Pb SHRIMP data for the zircon from the breccia thin section**

289 **72215,195.** a, Tera-Wasserburg concordia diagram. Data are not corrected for the
290 initial Pb. Blue ellipses represent the four oldest analyses; red ellipses represent the
291 five youngest analyses; yellow ellipses represent analyses with intermediate U-Pb
292 ages. b, Age vs. 'local misorientation' value determined at each SHRIMP spot from
293 EBSD map data by calculating the mean misorientation between a central point and
294 its nearest neighbours on an 11x11 pixel grid (i.e., 13.2x13.2 μm area)¹⁶. Local
295 misorientation data were normalised to alpha dose to account for the radiation
296 damage. The resultant local misorientation values are interpreted to reflect lattice
297 distortions associated with crystal-plastic deformation.

298

299 **Figure 3. LMO crystallisation paths based on the available chronological data.**
300 Solid line projected through the points representing 1) initial formation (100% melt –
301 ^{182}W age¹⁰), 2) mean time of lunar crust formation (30% melt – ^{143}Nd age⁵) 3) KREEP
302 formation (5-7% melt – age from this study), 4) time of cessation of magmatic activity
303 in the Serenitatis region (2.5-3.5% melt – age estimate from zircon distribution
304 patterns¹⁴); dotted line based on 1) and 2) and the assumption of a turbulent
305 convection in the LMO resulting in the fast initial cooling, yellow circle represents
306 predicted formation of the lunar crust compatible with such fast cooling of the LMO.
307

Figure 1

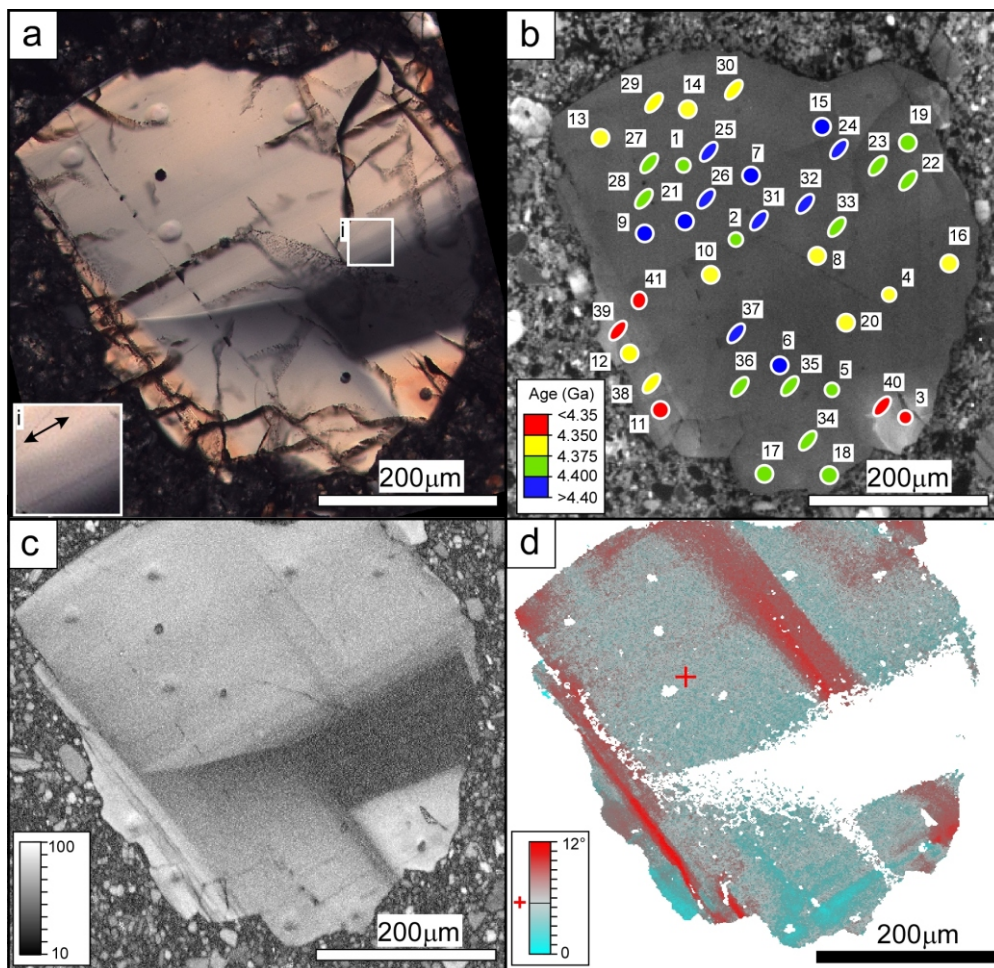


Figure 2

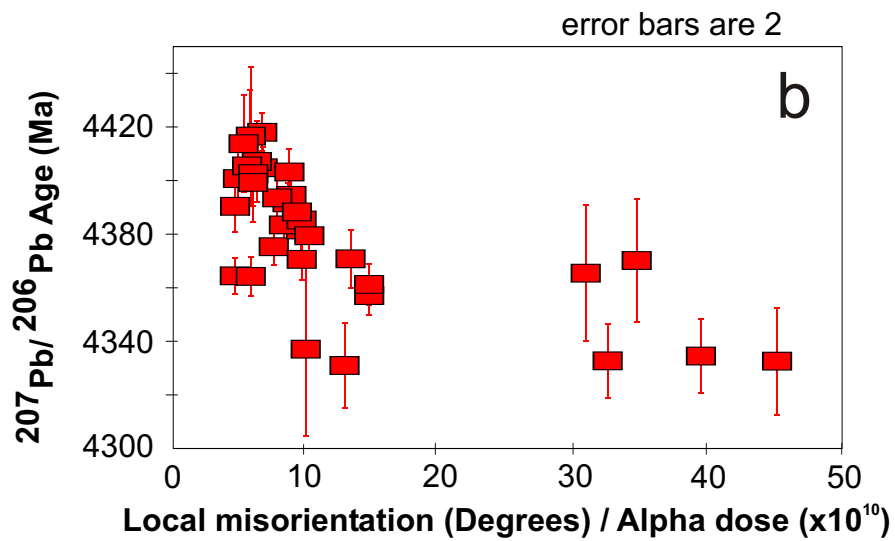
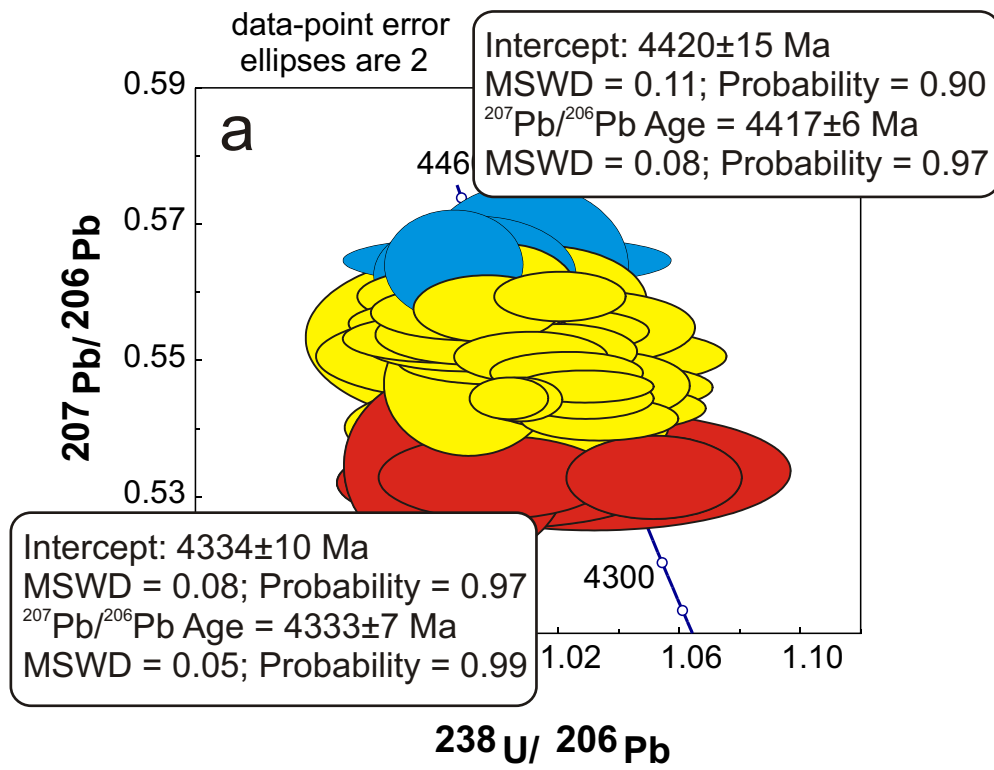
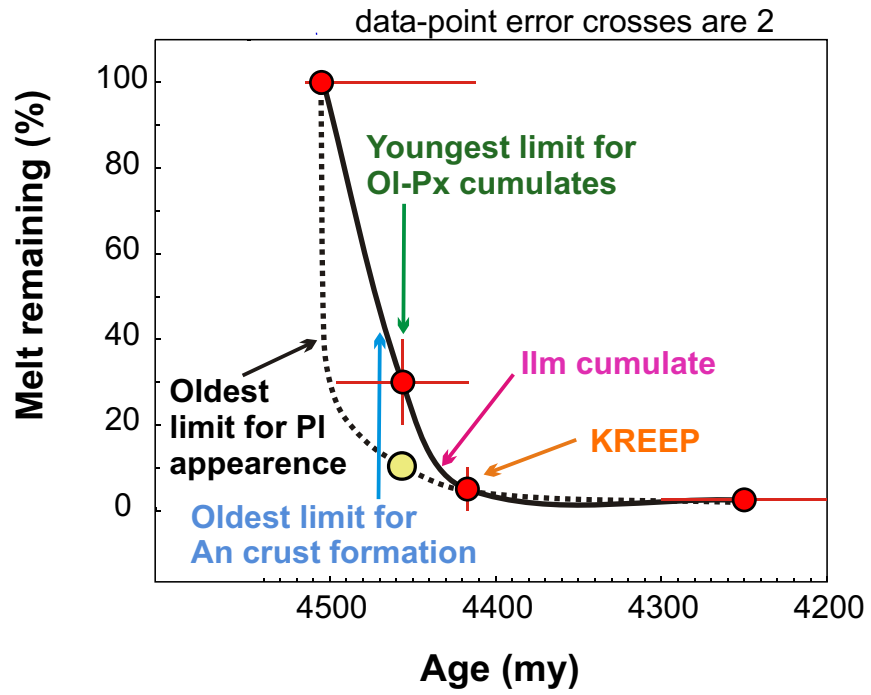


Figure 3



SUPPLEMENTARY MATERIALS

Methods

Cathodoluminescence

The panchromatic cathodoluminescence (CL) image was collected using a KE Developments CL system attached to a Philips XL30 SEM at the Microstructural Analysis Facility, Curtin University of Technology, Perth, Western Australia. Operating conditions were 12kV accelerating voltage and working distance of 15mm. The detector sensitivity is in the 330-600nm spectral range.

Electron backscatter diffraction (EBSD)

Prior to EBSD analysis, the sample was given an additional polish with 0.06 μ m colloidal silica NaOH (pH 9.8) suspension using a Buehler Vibromet II polisher for 4 hours to remove the surface damage from previous mechanical polishing, and given a thin (~1nm) carbon coat to reduced the effects of charging in the SEM chamber. Quantitative crystallographic orientation data was collected using EBSD via a Nordlys I detector attached to the Phillips XL30 SEM (20kV accelerating voltage, 20mm working distance, 70° tilt) at Curtin University, and processed using Oxford Instruments Channel 5 (SP9) software following the procedures described in detail for zircon²². Electron backscatter patterns (EBSPs) were collected (60 ms per frame, 4 frames noise reduction) on a user defined grid (464 x 487 pixels, 1.2 μ m spacing) and indexed using 8 detected bands; Hough resolution of 65, and match units derived from zircon crystal parameters obtained at 1 atm²³ (Mincrust record: Zircon [2])²⁴ following detailed assessment of these parameters²². Some domains of the grain yielded poor quality EBSPs and were unable to be indexed. The average “mean angular deviation” for indexed points is 0.72°. Band contrast is a measure of the EBSP pattern quality (i.e., EBSPs with faint Kikuchi bands yield low band contrast values), and values were obtained from the contrast between the 8 detected bands and the background in a Hough transformation of the EBSPs²².

Slip systems were resolved from EBSD data using a simple geometric approach that relates the geometry of low-angle tilt and twist boundaries and the dislocations responsible for their formation^{21, 25-27}. The map trace of the boundary and the crystallographic dispersion axis were used to reconstruct the 3D boundary orientation, and in turn relate the boundary and dispersion axis orientation to dislocation slip plane and slip direction by assuming end-member tilt boundary models.

Sensitive high-resolution ion microprobe (SHRIMP).

Isotopic data were collected using the Sensitive High Resolution Ion Microprobe (SHRIMP II) based in the John de Laeter Centre of Mass Spectrometry, Perth, Western Australia. The SHRIMP methodology follows analytical procedure described elsewhere¹³. The filtered (O_2^-) beam with intensity between 2 and 3 nA was focused on the surface of samples into $\sim 20 \mu m$ spot. Secondary ions were passed to the mass spectrometer operating at a mass resolution ($M/\Delta M$) of ~ 5000 . Each analysis was preceded by a 2 minute raster to remove the Au coating. The peak-hopping data collection routine consisted of five scans through the mass stations, with signals measured by an ion counting electron multiplier. Pb-U ratios were calibrated using an empirical correlation between Pb^+-U^+ and UO^+-U^+ ratios, normalised to the 564 Myr Sri-Lankan zircon CZ3 (Ref. 28). The 0.4 to 1.4% error obtained from the multiple analyses of Pb-U ratio on the standard during individual SHRIMP sessions was added in quadrature to the errors observed in the unknowns. The initial data reduction was done using the SQUID add-in for Microsoft Excel²⁹, and Isoplot³⁰ was applied for further age calculations.

The initial Pb correction of lunar samples is complicated by the highly radiogenic Pb compositions of many lunar rocks^{31, 320}, which suggest a substantial early loss of Pb from the Moon. A systematic change of $^{206}Pb/^{204}Pb$ during SHRIMP analyses of lunar zircon was used to suggest surface contamination as a result of smearing of Pb from the surrounding sample over the zircon surface

during polishing³³. However, recent study of 14 thin sections representing different breccia samples from the Apollo 14 and 17 landing sites suggests that although most of the common Pb is a surface contamination, its composition is most similar to the terrestrial Pb (Ref. 14). Therefore, U-Pb analyses obtained for the zircon from the thin section 72215,195 were corrected using modern Stacey and Kramers Pb (Ref. 34). Regardless, of the selection of common Pb for the correction, very low proportion of ²⁰⁴Pb in the thin section 72215,195 makes the calculated ages insensitive to the uncertainty in the common Pb.

Internal features of zircon from the breccia thin section 72215,195

The grain contains several domains, evident from differences in birefringence in cross polarized light (Fig. 1a). These domains have significantly different concentrations of U and Th, which has led to a different degree of self-irradiation damage across the grain. The most U- and Th-rich domain, with U and Th concentrations of ~150 and ~100 ppm respectively and highest Th/U of 0.64 to 0.67 (Tab. 1), also shows very low cathodoluminescence (CL) emission and poor electron backscatter diffraction (EBSD) pattern quality (Fig. 1). Several discrete domains that occur along the edge of the grain, are moderately luminescent and have good EBSD pattern quality (Fig. 1b and c), indicating that the lattice is crystalline. These domains are characterized by low U and Th concentration (~30 to 50 ppm and ~10 to 20 ppm) and the lowest Th/U (0.34 to 0.42, with only one analysis at 0.57). The rest of the grain is dominated by two domains with intermediate U and Th content (~100 to 70 ppm and ~70 to 40 ppm), Th/U (0.56 to 0.60), CL intensity and EBSD pattern quality (Fig. 1b and c). One of these domains records fine scale variations in birefringence (Fig. 1a, insert), interpreted to reflect primary (magmatic) growth zoning with associated minor chemical variation.

Crystallographic orientation analysis reveals that the zircon contains several deformation bands that transect primary zoning and predate brittle fractures (Fig. 1d). Two orthogonal sets of straight discrete and gradational low-angle boundaries accommodate ~12° misorientation across the

grain. The deformation bands are parallel to the crystallographic a -planes $\{010\}$ of the zircon, have misorientation axes parallel to the c -axis, and are geometrically consistent with formation by dislocation creep associated with $\langle 100 \rangle \{010\}$ slip²¹. The deformation bands are geometrically similar to dislocation microstructures reported in experimentally shocked zircon³⁵. We interpret these crystal-plastic deformation microstructures to have resulted from a significant impact, either directly from impact shock, or during ductile flow directly following the impact. The deformation bands appear to continue undeflected through the non-indexed, radiation-damaged areas of the grain, which indicates that the orientation variation predates any significant mechanical weakening from radiation damage in the grain, and therefore occurred early in its history. Crosscutting relationships between the deformation bands and the major chemical domains, identified within the grain, also demonstrate that the observed variation in U concentration and Th/U predate deformation and is the primary growth feature of this zircon.

References

22. Reddy, S.M., Timms, N.E. & Eglington, B., Electron backscatter diffraction analysis of zircon: A systematic assessment of match unit characteristics and pattern indexing optimization, *Am. Mineral.*, **93**, 197-197, 2008.
23. Hazen R.M. & Finger L.W. Crystal structure and compressibility of zircon at high pressure. *Am. Mineral.* **64**:196-201, 1979.
24. Chichagov, A.V., Varlamov, D.A., Dilanyan, R.A., Dokina, T.N., Drozhzhina, N.A., Samokhvalova, O.L., Ushakovskaya, T.V. MINCRYST: a Crystallographic Database for Minerals, Local and Network (WWW) Versions. *Crystallography Reports* **46**:876-879, 2001.

25. Lloyd, G.E., Farmer, A.B. & Mainprice, D. Misorientation analysis and the formation and orientation of subgrain and grain boundaries. *Tectonophysics* **279**:55-78, 1997.
26. Boyle, A.P., Prior, D.J., Banham, M.H. & Timms, N.E. Plastic deformation of metamorphic pyrite: new evidence from electron backscatter diffraction and foreshatter orientation-contrast imaging. *Mineral. Depos.* **34**:71-81, 1998.
27. Prior, D.J., Wheeler, J., Peruzzo, L., Spiess, R. & Storey C. Some garnet microstructures: an illustration of the potential of orientation maps and misorientation analysis in microstructural studies. *J. Struct. Geol.* **24**:999-1011, 2002.
28. Pidgeon, R.T., Furfaro, D., Kennedy, A.K., Nemchin, A.A., & van Bronswijk, W. Calibration of zircon standards for the Curtin SHRIMP, *In: 8th Int. Conf. on Geochronology, Cosmochronology and Isotope Geology, Berkeley, U.S. Geol. Surv. Circ. 1107*, p. 251, 1994.
29. Ludwig, K. Users manual for Squid1.02, *Berkeley Geochronology Center, Special Publication 1a*, 19pp, 2001a.
30. Ludwig, K. Users manual for Isoplot/Ex rev. 2.49, *Berkeley Geochronology Center, Special Publication 2*, 55pp., 2001a.
31. Tera, F. & Wasserburg, G. J., U-Th-Pb systematics in three Apollo 14 basalts and the problem of initial Pb in lunar rocks, *Earth Planet. Sci. Lett*, **14**, 281-304, 1972.
32. Gale, N. H. Uranium-lead systematics in lunar basalts, *Earth Planet. Sci. Lett*, **17**, 65-78, 1972.

33. Meyer, C., Williams, I.S. & Compston, W. Uranium-lead ages for lunar zircons: Evidence for a prolonged period of granophyre formation from 4.32 to 3.88 Ga. *Meteoritics Planet. Sci.* **31**, 370-387, 1996.
34. Stacey, J.S. & Kramers, J.D. Approximation of terrestrial lead isotope evolution by a two-stage model, *Earth Planet. Sci. Lett.* **26**, 207-221, 1975.
35. Leroux, H., Reimold, W.U., Koeberl, C., Hornemann, U. & Doukhan, J.C. Experimental shock deformation in zircon: a transmission electron microscopic study. *Earth Planet Sci Lett* **169**:291–301, 1999.

Table1. U-Pb SHRIMP data for the lunar zircon grain from the breccia thin section 72215,195

Spot	U (ppm)	Th (ppm)	$\frac{\text{Th}}{\text{U}}$	$\frac{^{204}\text{Pb}}{^{206}\text{Pb}}$	err ^a	$\frac{^{207}\text{Pb}}{^{206}\text{Pb}}$	err	$\frac{^{208}\text{Pb}}{^{206}\text{Pb}}$	err	$\frac{^{206}\text{Pb}}{^{238}\text{U}}$	err	$\frac{^{238}\text{U}^{\text{b}}}{^{206}\text{Pb}^*}$	err	$\frac{^{207}\text{Pb}^*}{^{206}\text{Pb}^*}$	err	disc ^c (%)	$\frac{^{207}\text{Pb}^*}{^{206}\text{Pb}^*}$ Age (Ma)
1	79	44	0.57	0.000127	27	0.5504	0.5	0.1422	0.9	1.005	2.3	0.998	2.3	0.5497	0.5	-2	4380±7
2	86	48	0.57	0.000086	52	0.5531	0.9	0.1452	0.9	1.009	2.2	0.993	2.3	0.5526	0.9	-2	4388±14
3	31	10	0.34	0.000257	34	0.5335	0.7	0.0925	1.7	0.969	2.6	1.037	2.6	0.5321	0.7	0	4333±10
4	151	94	0.65	0.000045	33	0.5400	0.5	0.1624	0.6	0.997	2.2	1.004	2.2	0.5397	0.5	-2	4354±8
5	106	61	0.59	0.000049	39	0.5504	0.4	0.1499	0.7	0.986	2.5	1.015	2.5	0.5501	0.4	-1	4381±5
6	105	61	0.60	0.000040	35	0.5592	0.3	0.1507	0.6	0.980	0.9	1.021	0.9	0.5590	0.3	0	4405±4
7	87	48	0.57	0.000060	37	0.5638	0.6	0.1413	0.7	1.015	0.9	0.986	0.9	0.5635	0.6	-2	4417±9
8	98	53	0.56	0.000084	24	0.5442	0.2	0.1390	0.8	0.996	0.5	1.005	0.5	0.5438	0.2	-2	4364±3
9	84	46	0.57	0.000058	39	0.5645	0.3	0.1393	0.8	0.997	2.2	1.004	2.2	0.5642	0.3	-1	4418±4
10	90	49	0.56	0.000064	32	0.5440	0.2	0.1386	0.7	0.993	0.6	1.008	0.6	0.5437	0.2	-2	4364±4
11	49	20	0.41	0.000031	46	0.5326	0.5	0.1024	0.8	0.951	1.1	1.052	1.1	0.5324	0.5	1	4334±7
12	52	20	0.40	0.000065	43	0.5462	0.8	0.1018	0.8	1.010	1.1	0.991	1.1	0.5459	0.8	-3	4370±12
13	78	44	0.58	0.000028	62	0.5412	0.2	0.1440	0.6	0.968	1.0	1.034	1.0	0.5410	0.2	0	4357±4
14	76	42	0.57	0.000010	53	0.5461	0.4	0.1425	0.6	0.964	1.0	1.037	1.0	0.5460	0.4	0	4371±5
15	84	46	0.57	0.000004	59	0.5598	0.5	0.1425	0.6	0.999	1.0	1.001	1.0	0.5598	0.5	-1	4407±8
16	151	94	0.64	0.000006	86	0.5460	0.2	0.1597	0.4	0.972	0.9	1.029	0.9	0.5459	0.2	0	4370±3
17	83	46	0.57	0.000019	46	0.5479	0.2	0.1405	0.6	0.978	1.0	1.023	1.0	0.5478	0.2	0	4375±3
18	79	45	0.59	0.000021	46	0.5503	0.3	0.1457	0.6	0.989	1.0	1.011	1.0	0.5501	0.3	-1	4382±4
19	83	46	0.57	0.000042	32	0.5511	0.3	0.1395	0.7	0.980	1.0	1.021	1.0	0.5509	0.3	0	4383±4
20	159	103	0.67	0.000009	74	0.5442	0.2	0.1652	0.4	0.972	0.9	1.029	0.9	0.5441	0.2	0	4365±3
21	87	48	0.57	0.000008	43	0.5574	0.4	0.1391	0.5	1.004	1.0	0.997	1.0	0.5573	0.4	-2	4400±5
22	86	48	0.58	0.000016	63	0.5541	0.3	0.1444	0.7	0.984	1.4	1.016	1.4	0.5540	0.3	-1	4392±4
23	83	47	0.58	0.000032	27	0.5552	0.3	0.1431	0.7	1.016	1.4	0.985	1.4	0.5550	0.3	-3	4395±4
24	86	47	0.56	0.000019	61	0.5591	0.3	0.1403	0.7	1.014	1.4	0.987	1.4	0.5590	0.3	-2	4405±5
25	79	45	0.59	0.000017	55	0.5582	0.6	0.1459	0.7	0.986	1.4	1.015	1.4	0.5581	0.6	0	4403±9
26	92	50	0.57	0.000009	53	0.5634	0.9	0.1390	0.8	0.991	1.4	1.009	1.4	0.5634	0.9	-1	4416±13

Table1. (continued)

Spot	U	Th	$\frac{\text{Th}}{\text{U}}$	$\frac{^{204}\text{Pb}}{^{206}\text{Pb}}$	err ^a	$\frac{^{207}\text{Pb}}{^{206}\text{Pb}}$	err	$\frac{^{208}\text{Pb}}{^{206}\text{Pb}}$	err	$\frac{^{206}\text{Pb}}{^{238}\text{U}}$	err	$\frac{^{238}\text{U}^b}{^{206}\text{Pb}^*}$	err	$\frac{^{207}\text{Pb}^*}{^{206}\text{Pb}^*}$	err	disc ^c	$\frac{^{207}\text{Pb}^*}{^{206}\text{Pb}^*}$ Age (Ma)
	(ppm)	(ppm)														(%)	
27	78	44	0.58	0.000026	47	0.5517	0.3	0.1443	0.7	1.010	1.4	0.990	1.4	0.5516	0.3	-3	4385±4
28	91	49	0.56	0.000015	83	0.5546	0.4	0.1375	0.8	0.971	1.4	1.030	1.4	0.5545	0.4	0	4393±6
29	73	41	0.58	0.000031	55	0.5427	0.3	0.1449	0.7	0.968	1.4	1.034	1.4	0.5426	0.3	0	4361±4
30	76	42	0.58	0.000043	37	0.5458	0.3	0.1440	0.7	0.965	1.4	1.037	1.4	0.5456	0.3	0	4369±4
31	85	48	0.58	0.000012	81	0.5624	0.6	0.1433	0.7	1.008	1.4	0.992	1.4	0.5623	0.6	-2	4413±9
32	85	48	0.58	0.000042	37	0.5581	0.3	0.1435	0.7	1.005	1.4	0.996	1.4	0.5579	0.3	-2	4402±4
33	87	49	0.58	0.000050	27	0.5529	0.3	0.1454	0.9	1.019	1.4	0.983	1.4	0.5527	0.3	-3	4388±4
34	80	46	0.59	0.000063	23	0.5497	0.3	0.1477	0.7	1.000	1.4	1.002	1.4	0.5493	0.3	-2	4379±4
35	93	53	0.59	0.000013	77	0.5535	0.3	0.1471	0.6	1.008	1.3	0.992	1.3	0.5535	0.3	-2	4390±5
36	100	54	0.56	0.000010	80	0.5568	0.3	0.1374	0.7	1.009	1.3	0.991	1.3	0.5568	0.3	-2	4399±4
37	119	69	0.60	0.000018	43	0.5584	0.2	0.1492	0.6	0.996	1.3	1.004	1.3	0.5583	0.2	-1	4403±3
38	51	21	0.42	0.000007	99	0.5442	0.9	0.1096	1.1	0.990	1.5	1.010	1.5	0.5441	0.9	-2	4365±13
39	35	14	0.41	0.000085	44	0.5326	0.5	0.1075	1.4	1.001	1.6	1.000	1.6	0.5321	0.5	-3	4333±7
40	41	16	0.40	0.000092	26	0.5342	1.1	0.0986	1.2	1.014	1.5	0.988	1.5	0.5337	1.1	-4	4337±16
41	84	46	0.57	0.000074	30	0.5318	0.5	0.1396	0.8	0.999	2.2	1.002	2.2	0.5314	0.5	-3	4331±8

^a all errors are % 1 sigma^b ²⁰⁶Pb* is radiogenic ²⁰⁶Pb^c % discordance